



Cite this: *CrystEngComm*, 2015, 17, 6098

Received 29th May 2015,
Accepted 3rd July 2015

DOI: 10.1039/c5ce01035g

www.rsc.org/crystengcomm

Topochemical transformation of low-energy crystal facets to high-energy facets: a case from $\text{Bi}_2\text{O}_2\text{CO}_3$ {001} facets to $\beta\text{-Bi}_2\text{O}_3$ {001} facets with improved photocatalytic oxidation of NO^\dagger

Fang Wang,^{ab} Ziyang Zhao,^b Kunhao Zhang,^c Fan Dong^d and Ying Zhou^{*ab}

Herein, $\beta\text{-Bi}_2\text{O}_3$ nanosheets exposed with active {001} facets were facilely prepared through annealing $\text{Bi}_2\text{O}_2\text{CO}_3$ with thermally stable {001} facets. The enhanced photocatalytic activity of $\beta\text{-Bi}_2\text{O}_3$ was ascribed to the high energy of {001} facets and the efficient charge separation. This 2D surface transformation strategy could shed new light on the fabrication of energetic facets and the development of highly active photocatalysts.

Since the successful synthesis of high energy {001} facets of anatase TiO_2 crystals using HF as a controlling agent,¹ semiconductor crystal-facet engineering has become a hot research topic in the pursuit of highly reactive faceted photocatalysts.² Generally, semiconductor crystals exposed with different facets have diverse physicochemical properties and result in very different catalytic activities. For instance, BiOCl nanosheets with exposed {001} facets exhibited enhanced photoactivity compared to their counterparts with {010} facets.³ The improved photocatalytic activity of Ag_3PO_4 rhombic dodecahedra has been ascribed to the higher energy of {110} facets (1.31 J m^{-2}) than that of {100} facets (1.12 J m^{-2}).⁴ However, controlling the crystal facets of semiconductors is still a tremendous challenge, which has only been achieved in limited material systems.^{1,5} So far, almost all of these semiconductors with controlled surface facets were obtained by hydrothermal methods.^{1–5} As the reactive facets diminish rapidly during the crystal growth due to the minimization of the surface energy, optimizing the reaction kinetics is crucial and may require considerable “trial and error”

work.⁶ Therefore, the predictive and rational preparation of a desired crystal facet is rather difficult. This calls for the development of a novel preparative strategy.

Sillén-type $\text{Bi}_2\text{O}_2\text{CO}_3$ is composed of alternating $\text{Bi}_2\text{O}_2^{2+}$ and CO_3^{2-} layers along the *c* axis. Consequently, $\text{Bi}_2\text{O}_2\text{CO}_3$ nanosheets dominated with {001} facets have been easily prepared by various groups.⁷ Meanwhile, metastable $\beta\text{-Bi}_2\text{O}_3$ has a closely related crystal structure to $\text{Bi}_2\text{O}_2\text{CO}_3$ because both of them contain the same atomic arrangement in their $\text{Bi}_2\text{O}_2^{2+}$ layers.⁸ Especially, the lattice misfit between the {110} facets of $\text{Bi}_2\text{O}_2\text{CO}_3$ and the {220} facets of $\beta\text{-Bi}_2\text{O}_3$ is only 0.1%,⁹ indicating that these two phases could be transformed to each other easily. It was found that even under room temperature, $\beta\text{-Bi}_2\text{O}_3$ can capture atmospheric CO_2 to form $\text{Bi}_2\text{O}_2\text{CO}_3$ nanosheets in our previous work.¹⁰ Meanwhile, $\text{Bi}_2\text{O}_2\text{CO}_3$ can be converted back to metastable $\beta\text{-Bi}_2\text{O}_3$ through releasing CO_2 by annealing.¹¹ Nevertheless, compared to $\text{Bi}_2\text{O}_2\text{CO}_3$, $\beta\text{-Bi}_2\text{O}_3$ nanosheets with exposed {001} facets have been seldom reported due to the high surface energy of {001} facets (1.83 J m^{-2}), which is higher than those of both {100} (0.98 J m^{-2}) and {110} (1.42 J m^{-2}) facets.¹²

In this work, we report a facile route to fabricate the energetic facet *via* lattice matching, *i.e.*, the reactive facet of one crystal can be prepared by another material with a thermodynamically stable facet through annealing. $\beta\text{-Bi}_2\text{O}_3$ and $\text{Bi}_2\text{O}_2\text{CO}_3$ were selected as model materials as they have close crystal structures and good lattice match. This concept could have a good universality in the synthesis of other highly reactive faceted materials and shed light on the development of highly active photocatalysts.

The detailed procedure for the theoretical calculations and experiments was described in the ESI.† Fig. S1 shows the structures of $\text{Bi}_2\text{O}_2\text{CO}_3$ and $\beta\text{-Bi}_2\text{O}_3$ with the side views of {001}, {110} and {010} facets. The surface free energies of these stoichiometric low-miller index surfaces for both $\text{Bi}_2\text{O}_2\text{CO}_3$ and $\beta\text{-Bi}_2\text{O}_3$ were computed through density functional theory (DFT) calculations. It was observed that the variation trend is the same for the surface free energies with and

^a State Key Laboratory of Oil and Gas Reservoir Geology and Exploitation, Southwest Petroleum University, Chengdu 610500, China.
E-mail: yzhou@swpu.edu.cn

^b The Center of New Energy Materials and Technology, School of Materials Science and Engineering, Southwest Petroleum University, Chengdu 610500, China

^c Shanghai Synchrotron Radiation Facility, Shanghai Institute of Applied Physics, Chinese Academy of Sciences, Shanghai 201204, China

^d College of Environmental and Biological Engineering, Chongqing Technology and Business University, Chongqing 400067, China

† Electronic supplementary information (ESI) available: Experimental details, and Fig. S1 to S5. See DOI: 10.1039/c5ce01035g

without surface relaxation (Table 1) in accordance with the previous theoretical surface study on bismuth oxides.¹³ The (001) facet of $\text{Bi}_2\text{O}_2\text{CO}_3$ has the lowest surface free energy compared to other planes, while for $\beta\text{-Bi}_2\text{O}_3$ the (001) facet exhibits the highest surface free energy. Therefore, it is proved that the experimental preparation of $\beta\text{-Bi}_2\text{O}_3$ with energetic {001} facets is much more difficult than that of $\text{Bi}_2\text{O}_2\text{CO}_3$ with thermodynamically stable {001} facets. Fig. 1 highlights the structure details related to atomic arrangements. It is interesting to note that they have a common structural feature along the (001) plane. The atomic array of $\text{Bi}_2\text{O}_2^{2+}$ layer in $\text{Bi}_2\text{O}_2\text{CO}_3$ is also the same fragment existing in $\beta\text{-Bi}_2\text{O}_3$, which means that the Bi and O atom fragments in $\text{Bi}_2\text{O}_2^{2+}$ of $\text{Bi}_2\text{O}_2\text{CO}_3$ are prone to rearrange to form $\beta\text{-Bi}_2\text{O}_3$ along the (001) facet after releasing CO_2 . The two-dimensional (2D) surface transformation along the (001) plane could result in the same lattice arrays for $\text{Bi}_2\text{O}_2\text{CO}_3$ and $\beta\text{-Bi}_2\text{O}_3$. Therefore, $\beta\text{-Bi}_2\text{O}_3$ nanosheets with active {001} facets could be prepared from the easily accessed $\text{Bi}_2\text{O}_2\text{CO}_3$ with exposed {001} facets.

Inspired by the theoretical calculations, $\text{Bi}_2\text{O}_2\text{CO}_3$ (BOC) particles were prepared through modifying a reported method.¹⁴ The TG curve (Fig. S2†) reveals that the obtained BOC samples start to decompose at 340 °C and *ca.* 8% weight loss is observed, matching well with the theoretical weight loss (8.6%) due to the release of CO_2 . Consequently, the obtained samples were annealed under atmospheric conditions at 350, 380, 400 and 420 °C, respectively, which are denoted as BOC-350, BOC-380, BOC-400 and BOC-420. Fig. S3† shows the PXRD patterns of these samples. All diffraction peaks of the prepared BOC can be indexed into the tetragonal $\text{Bi}_2\text{O}_2\text{CO}_3$ (JCPDS no. 41-1488). Although tetragonal $\beta\text{-Bi}_2\text{O}_3$ was already formed at 350 °C, BOC-350 is still dominated by $\text{Bi}_2\text{O}_2\text{CO}_3$ phase. With the further increase in temperature, the ratio of $\beta\text{-Bi}_2\text{O}_3$ in the products (BOC-380 and BOC-400) increased. Finally, $\text{Bi}_2\text{O}_2\text{CO}_3$ was completely converted to $\beta\text{-Bi}_2\text{O}_3$ phase (BOC-420) at 420 °C. In addition, a small amount of $\text{Bi}_2\text{O}_{2.33}$ was observed as well. As $\beta\text{-Bi}_2\text{O}_3$ is a metastable phase, it could be converted to the thermodynamically stable $\alpha\text{-Bi}_2\text{O}_3$ phase at higher annealing temperature.¹⁵ In line with the PXRD patterns, the UV-vis absorption spectra of these samples also varied with temperature (Fig. S4†). The band gaps (E_g) of BOC, BOC-350, BOC-380, BOC-400 and BOC-420 were determined as 3.55, 3.29, 2.58, 2.52 and 2.52, respectively, according to the onset of the absorption edge. The E_g of BOC matched well with the previously reported

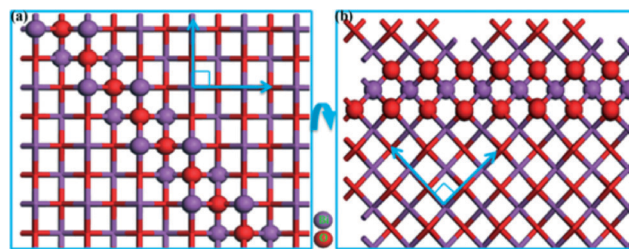


Fig. 1 Atomic arrays of $\text{Bi}_2\text{O}_2^{2+}$ layers of (a) $\text{Bi}_2\text{O}_2\text{CO}_3$ and (b) $\beta\text{-Bi}_2\text{O}_3$ top-viewed along (001) facet.

value for $\text{Bi}_2\text{O}_2\text{CO}_3$,¹⁶ whereas the E_g of these samples decreased with the annealing temperature as the E_g of $\beta\text{-Bi}_2\text{O}_3$ is much smaller than that of $\text{Bi}_2\text{O}_2\text{CO}_3$.¹⁷

To gain insight into the chemical states of the elements on the surface of BOC and BOC-420, XPS spectra were obtained. Both samples contained Bi, O and C in the survey spectra (Fig. 2a). Fig. 2b shows two strong symmetrical peaks at *ca.* 164.4 and 159.1 eV, corresponding to Bi 4f_{5/2} and Bi 4f_{7/2} signals from the Bi^{3+} ions of both samples.¹⁸ Fig. 2c displays the O 1s spectra of BOC and BOC-420. A broad peak ranging from 529 to 534 was observed, which can be fitted by three peaks at the binding energies of 530.6, 531.6 and 532.6 eV for BOC or 530.1, 531.1 and 531.8 eV for BOC-420. The peak at 530.6 (530.1) eV can be ascribed to the oxygen of the Bi–O bond, while the other two peaks are from the lattice oxygen, carbonate species and adsorbed H_2O on the surface.¹⁹ The peaks for C 1s located at 284.8, 285.6 and 286.7 eV are ascribed to adventitious carbon species from the XPS instrument, whereas the peak at 289.0 eV can be assigned to the carbon in the CO_3^{2-} group (Fig. 2d).²⁰ These results revealed that even after annealing at 420 °C, the surface of BOC-420 still contained CO_3^{2-} , which could play an important role in the stabilization of metastable $\beta\text{-Bi}_2\text{O}_3$. Previously, Jiang *et al.* found that $\beta\text{-Bi}_2\text{O}_3$ was converted to thermally stable $\alpha\text{-Bi}_2\text{O}_3$

Table 1 Calculated surface energies (in J m^{-2}) with and without surface relaxation of various facets for $\text{Bi}_2\text{O}_2\text{CO}_3$ and $\beta\text{-Bi}_2\text{O}_3$

Crystal	(001)	(110)	(010)
$\text{Bi}_2\text{O}_2\text{CO}_3$	1.23 (1.01) ^a	1.37 (1.00)	1.79 (1.15)
$\beta\text{-Bi}_2\text{O}_3$	1.96 (0.57)	1.43 (0.21)	1.44 (0.22)

^a Data in parentheses refer to the surface energy with surface relaxation.

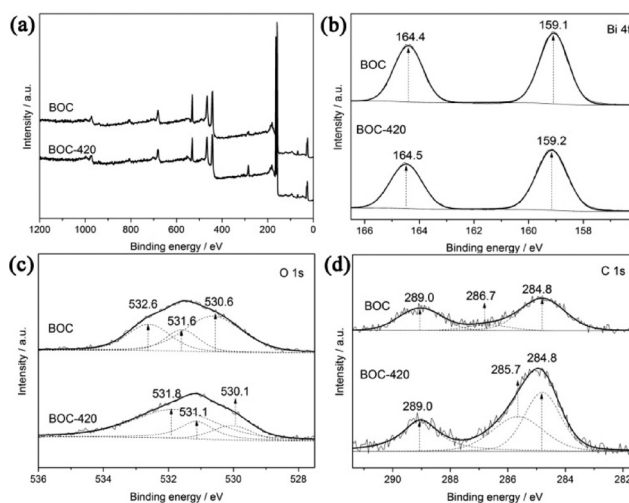


Fig. 2 XPS spectra of (a) survey; (b) Bi 4f; (c) O 1s; (d) C 1s for BOC and BOC-420.

phase once the remaining surface-coordinated CO_3^{2-} was not enough to stabilize the crystal structure of $\beta\text{-Bi}_2\text{O}_3$.¹⁵

The morphology and microstructure of these samples were further investigated by SEM and TEM observations. The prepared BOC is constituted by large amounts of nanosheets with a thickness of *ca.* 30 nm (Fig. 3a and b). Annealing at 420 °C did not significantly change the morphology and size of the products. Hence, BOC-420 could maintain the 2D morphology of BOC (Fig. 3c and d). The TEM images (Fig. 4a and c) further confirmed the similar 2D morphology for both BOC and BOC-420. The BET surface areas of BOC and BOC-420 were determined as 14.3 and 5.9 $\text{m}^2 \text{g}^{-1}$, respectively. The HRTEM image of BOC (Fig. 4b) shows clear lattice fringes with an interplanar lattice spacing of 0.274 nm and an angle of 90°, which is consistent with the (110) planes of the tetragonal $\text{Bi}_2\text{O}_2\text{CO}_3$. The corresponding SAED pattern (inset of Fig. 4b) indicates the single-crystal nature of BOC, which can be indexed as the [001] zone axis. Both HRTEM and SAED results confirmed that the top and bottom exposed surfaces of BOC are {001} facets. According to Fig. 1, $\beta\text{-Bi}_2\text{O}_3$ and $\text{Bi}_2\text{O}_2\text{CO}_3$ have similar atomic arrays of $\text{Bi}_2\text{O}_2^{2+}$ layers along (001) facets. Hence, $\beta\text{-Bi}_2\text{O}_3$ with active {001} facets could be transformed from $\text{Bi}_2\text{O}_2\text{CO}_3$ with exposed {001} facets through annealing. Fig. 4d shows the HRTEM image of BOC-420. A lattice fringe of 0.274 nm was observed, corresponding to the interplanar spacing of the (220) of tetragonal $\beta\text{-Bi}_2\text{O}_3$. The angle of adjacent spots marked in the SAED pattern is 45°, matching well with the theoretical value of the angle between the (220) and (200) planes of $\beta\text{-Bi}_2\text{O}_3$. Therefore, the set of diffraction spots can be assigned to the [001] zone-axis diffraction spots of $\beta\text{-Bi}_2\text{O}_3$, revealing that $\beta\text{-Bi}_2\text{O}_3$ nanosheets with exposed {001} facets have been successfully obtained through annealing $\text{Bi}_2\text{O}_2\text{CO}_3$ nanosheets with {001} facets at 420 °C. We believe that the lattice match between the {110} facets of $\text{Bi}_2\text{O}_2\text{CO}_3$ and the {220} facets of $\beta\text{-Bi}_2\text{O}_3$ is the main reason for the formation of $\beta\text{-Bi}_2\text{O}_3$ with active {001} facets. On the other hand, the CO_3^{2-} content on the

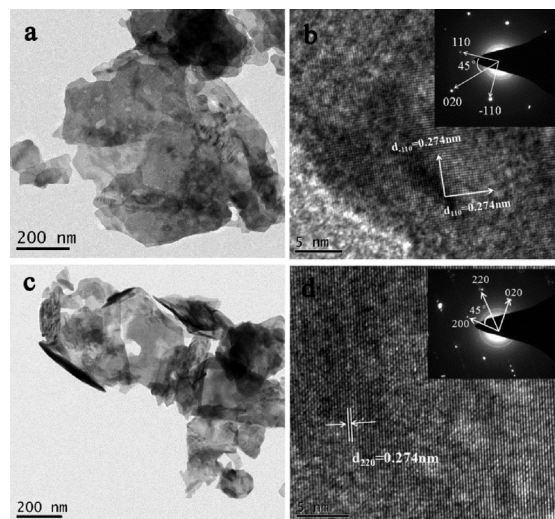


Fig. 4 TEM images of (a) BOC and (c) BOC-420; HRTEM images of (b) BOC and (d) BOC-420 (insets are the corresponding SAED patterns).

surface of $\beta\text{-Bi}_2\text{O}_3$ (Fig. 2d) may also play an important role, which can lower the surface energy of $\beta\text{-Bi}_2\text{O}_3$.¹⁵ Similar phenomenon has been reported in other material systems. For example, anatase TiO_2 with active {001} facets can be prepared in the presence of F^- because the surface adsorbed F^- is effective in lowering the surface energy of the {001} surface of anatase TiO_2 .^{1,2,21}

The photocatalytic activity of these samples was evaluated by photocatalytic oxidation of ppb-level NO in air under UV-visible and visible light ($\lambda > 420 \text{ nm}$) irradiation. As shown in Fig. 5, after 30 min irradiation, the NO removal ratio of BOC under UV-visible light is 41%, while it is only 19% under visible light irradiation due to the large band gap (Fig. S4†). The photocatalytic behaviour of BOC-400 is similar to that of BOC. Importantly, BOC-420 exhibits significantly enhanced NO removal efficiency especially under visible light irradiation. The NO removal ratio over BOC-420 can reach as high as 54% or 40% after 30 min UV-visible light or visible light irradiation, respectively. Generally, a conventional TiO_2 (P25) photocatalyst exhibited almost no photocatalytic NO oxidation activity under visible light irradiation due to its wide band gap. Using the same reactor, the photodegradation ratio of NO over P25 under UV light after 30 min irradiation

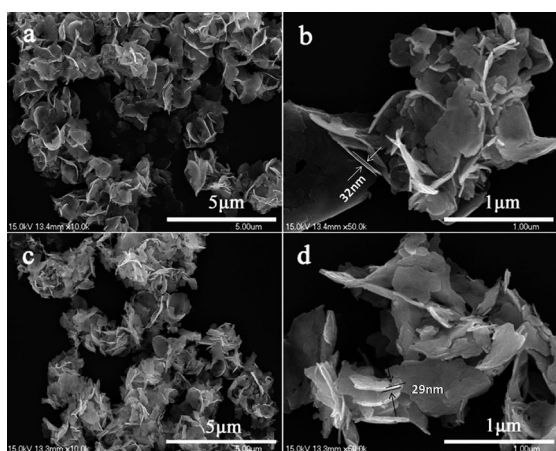


Fig. 3 Representative SEM images of (a) BOC (low magnification); (b) BOC (high magnification); (c) BOC-420 (low magnification); (d) BOC-420 (high magnification).

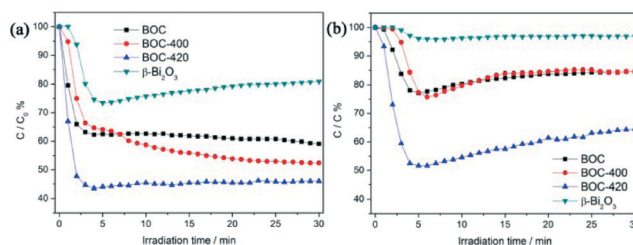


Fig. 5 Photocatalytic activities of the prepared samples and commercial $\beta\text{-Bi}_2\text{O}_3$ nanoparticles as the reference under (a) UV-visible light and (b) visible light ($\lambda > 420 \text{ nm}$) irradiation.

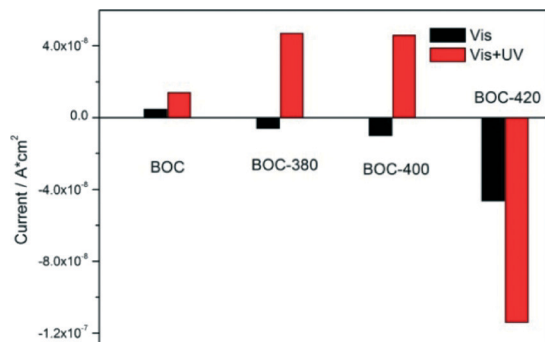


Fig. 6 Photocurrent of the obtained samples under UV-visible light and visible light ($\lambda > 420$ nm) irradiation.

is 38%.¹⁹ Moreover, the commercial β - Bi_2O_3 particles (Sigma-Aldrich) with a particle size range of 90–210 nm and a BET surface area of 3.2–3.5 $\text{m}^2 \text{g}^{-1}$ were taken as a reference to compare their activity with the prepared β - Bi_2O_3 with active {001} facets. Fig. S5† shows the XRD and SEM images of the commercial particles. The commercial β - Bi_2O_3 particles exhibited a much lower photocatalytic activity compared to BOC-420 both under UV-visible light and visible light irradiation (Fig. 5). All in all, these results confirmed that the prepared β - Bi_2O_3 exhibited enhanced photocatalytic activity towards NO oxidation, which could be attributed to the high energy of {001} facets (1.96 J m^{-2}) (Table 1), given that both BOC and BOC-420 have similar morphologies and particle sizes (Fig. 3).

Photocurrent measurements were further performed to investigate the interfacial charge transfer behaviours.²² All of these experiments were measured in a standard three-electrode photoelectrochemical cell (ESI†). BOC exhibited anodic photocurrent generation under both UV-visible light and visible light irradiation, indicating their n-type semiconductor behaviours (Fig. 6). In line with its wide band gap (Fig. S4†), the photocurrent of BOC under visible light is very low. However, BOC-380 and BOC-400 exhibited different behaviours. Under visible light irradiation, both of them displayed cathodic photocurrent, revealing their p-type semiconductor properties (Fig. 6). β - Bi_2O_3 is a p-type semiconductor.²³ Hence, under visible light irradiation, only the formed β - Bi_2O_3 was activated. Under UV-visible light, an anodic photocurrent was observed for both samples. Consequently, although both $\text{Bi}_2\text{O}_2\text{CO}_3$ and β - Bi_2O_3 can be activated under UV-visible light, the photocurrent was dominated by that from $\text{Bi}_2\text{O}_2\text{CO}_3$. As $\text{Bi}_2\text{O}_2\text{CO}_3$ is an n-type semiconductor, the formation of β - Bi_2O_3 and $\text{Bi}_2\text{O}_2\text{CO}_3$ p–n heterojunctions could reduce the recombination rate of photogenerated electrons and holes, thus resulting in enhanced anodic photocurrent compared to the pristine $\text{Bi}_2\text{O}_2\text{CO}_3$.²⁴ After annealing at 420 °C, $\text{Bi}_2\text{O}_2\text{CO}_3$ decomposed completely (Fig. S3†). Therefore, only cathodic photocurrent was observed for BOC-420 regardless of UV-visible light or visible light irradiation. Besides, BOC-420 exhibited the highest photocurrent among the studied samples, confirming that β - Bi_2O_3 with

active {001} facets also revealed more efficient charge separation compared to $\text{Bi}_2\text{O}_2\text{CO}_3$.

Conclusions

In summary, we report a facile route to prepare β - Bi_2O_3 nanosheets with active {001} facets through annealing $\text{Bi}_2\text{O}_2\text{CO}_3$ nanosheet precursor. The lattice match between the {110} facets of $\text{Bi}_2\text{O}_2\text{CO}_3$ and the {220} facets of β - Bi_2O_3 as well as the CO_3^{2-} content on the surface could be the reason for the formation of β - Bi_2O_3 with active {001} facets. The prepared β - Bi_2O_3 nanosheets exhibited enhanced photocatalytic activity toward NO oxidation, both under UV-visible light and visible light irradiation due to the high energy of {001} facets (1.96 J m^{-2}) and the more efficient charge separation. This strategy is expected to be applicable for preparing other materials with active facets for photocatalytic applications.

Acknowledgements

This research was funded by the National Natural Science Foundation of China (U1232119), Sichuan Youth Science and Technology Foundation (2013JQ0034, 2014JQ0017), the Scientific Research Starting project of SWPU (2014QHZ020, 2014QHZ021, 2014PYZ012), and the Innovative Research Team of Sichuan Provincial Education Department and SWPU (2012XJZT002).

Notes and references

- H. G. Yang, C. H. Sun, S. Z. Qiao, J. Zou, G. Liu, S. C. Smith, H. M. Cheng and G. Q. Lu, *Nature*, 2008, **453**, 638.
- (a) G. Liu, J. C. Yu, G. Q. Lu and H. M. Cheng, *Chem. Commun.*, 2011, **47**, 6763; (b) G. Liu, H. G. Yang, J. Pan, Y. Q. Yang, G. Q. Lu and H. M. Cheng, *Chem. Rev.*, 2014, **114**, 9559.
- J. Jiang, K. Zhao, X. Y. Xiao and L. Z. Zhang, *J. Am. Chem. Soc.*, 2012, **134**, 4473.
- Y. P. Bi, S. X. Ouyang, N. Umezawa, J. Y. Cao and J. H. Ye, *J. Am. Chem. Soc.*, 2011, **133**, 6490.
- (a) Y. P. Xie, G. Liu, L. C. Yin and H. M. Cheng, *J. Mater. Chem.*, 2012, **22**, 6746; (b) R. G. Li, F. X. Zhang, D. Wang, J. X. Yang, M. R. Li, J. Zhu, X. Zhou, H. X. Han and C. Li, *Nat. Commun.*, 2013, **4**, 1432; (c) J. L. Long, S. C. Wang, H. J. Chang, B. Z. Zhao, B. T. Liu, Y. G. Zhou, W. Wei, X. X. Wang, L. Huang and W. Huang, *Small*, 2014, **10**, 2791; (d) J. M. Peng, Y. Zhou, H. Wang, H. R. Zhou and S. Y. Cai, *CrystEngComm*, 2015, **17**, 1805.
- (a) K. Byrappa and T. Adschin, *Prog. Cryst. Growth Charact. Mater.*, 2007, **53**, 117; (b) G. R. Patzke, Y. Zhou, R. Kontic and F. Conrad, *Angew. Chem., Int. Ed.*, 2011, **50**, 826; (c) Y. Zhou, N. Pienack, W. Bensch and G. R. Patzke, *Small*, 2009, **5**, 1978; (d) Y. Zhou, E. Antonova, W. Bensch and G. R. Patzke, *Nanoscale*, 2010, **2**, 2412.
- (a) Y. Zheng, F. Duan, M. Q. Chen and Y. Xie, *J. Mol. Catal. A: Chem.*, 2010, **317**, 34; (b) H. W. Huang, J. J. Wang, F. Dong, Y. X. Guo, N. Tian, Y. H. Zhang and T. R. Zhang,

- Cryst. Growth Des.*, 2015, 15, 534; (c) Z. Y. Zhao, Y. Zhou, F. Wang, K. H. Zhang, S. Yu and K. Cao, *ACS Appl. Mater. Interfaces*, 2015, 7, 730; (d) H. W. Huang, X. W. Li, J. J. Wang, F. Dong, P. K. Chu, T. R. Zhang and Y. H. Zhang, *ACS Catal.*, 2015, 5, 4094; (e) D. D. Hu, K. Y. Zhang, Q. Yang, M. J. Wang, Y. Xi and C. G. Hu, *Appl. Surf. Sci.*, 2014, 316, 93.
- 8 C. Greaves and S. K. Blower, *Mater. Res. Bull.*, 1988, 23, 1001.
 - 9 C. F. Guo, J. M. Zhang, Y. Tian and Q. Liu, *ACS Nano*, 2012, 6, 8746.
 - 10 Y. Zhou, H. Y. Wang, M. Sheng, Q. Zhang, Z. Y. Zhao, Y. H. Lin, H. F. Liu and G. R. Patzke, *Sens. Actuators, B*, 2013, 188, 1312.
 - 11 G. Q. Zhu, J. Lian, M. Hojamberdiev and W. X. Que, *J. Cluster Sci.*, 2013, 24, 829.
 - 12 H. Liu, M. Luo, J. C. Hu, T. F. Zhou, R. Chen and J. L. Li, *Appl. Catal., B*, 2013, 140–141, 141.
 - 13 Y. H. Lei and Z. X. Chen, *J. Chem. Phys.*, 2013, 138, 054703.
 - 14 L. Chen, R. Huang, S. F. Yin, S. L. Luo and C. T. Au, *Chem. Eng. J.*, 2012, 193–194, 123–130.
 - 15 H.-Y. Jiang, P. Li, G. G. Liu, J. H. Ye and J. Lin, *J. Mater. Chem. A*, 2015, 3, 5119.
 - 16 (a) P. Madhusudan, J. R. Ran, J. Zhang, J. G. Yu and G. Liu, *Appl. Catal., B*, 2011, 110, 286; (b) X. F. Cao, L. Zhang, X. T. Chen and Z. L. Xue, *CrystEngComm*, 2011, 13, 1939; (c) S. Q. Liu, Y. Q. Tu and G. D. Dai, *Ceram. Int.*, 2014, 40, 2343.
 - 17 M. N. Gómez-Cerezo, M. J. Muñoz-Batista, D. Tudela, M. Fernández-García and A. Kubacka, *Appl. Catal., B*, 2014, 156–157, 307.
 - 18 S. Shamaila, A. K. L. Sajjad, F. Chen and J. L. Zhang, *Appl. Catal., B*, 2010, 94, 272.
 - 19 F. Dong, S. C. Lee, Z. B. Wu, Y. Huang, M. Fu, W.-K. Ho, S. C. Zou and B. Wang, *J. Hazard. Mater.*, 2011, 195, 346.
 - 20 (a) P. Madhusudan, J. Yu, W. Wang, B. Cheng and G. Liu, *Dalton Trans.*, 2012, 41, 14345; (b) P. Madhusudan, J. Zhang, B. Cheng and G. Liu, *CrystEngComm*, 2013, 15, 231.
 - 21 S. W. Liu, J. G. Yu and M. Jaroniec, *Chem. Mater.*, 2011, 23, 4085.
 - 22 (a) H. Kim, P. Borse, W. Choi and J. Lee, *Angew. Chem., Int. Ed.*, 2005, 44, 4485; (b) Q. Zhang, Y. Zhou, F. Wang, F. Dong, W. Li, H. M. Li and G. R. Patzke, *J. Mater. Chem. A*, 2014, 2, 11065.
 - 23 A. Cabot, A. Marsal, J. Arbiol and J. R. Morante, *Sens. Actuators, B*, 2004, 99, 74.
 - 24 (a) R. P. Hu, X. Xiao, S. H. Tu, X. X. Zuo and J. M. Nan, *Appl. Catal., B*, 2015, 163, 510; (b) G. Y. Cai, L. L. Xu, B. Wei, J. X. Che, H. Gao and W. J. Sun, *Mater. Lett.*, 2014, 120, 1.